PAPER • OPEN ACCESS

Prospects of temperature performance enhancement through higher resonant phonon transition designs in GaAs-based terahertz quantum-cascade lasers

To cite this article: Aleksandar Demić *et al* 2022 *New J. Phys.* **24** 033047

View the article online for updates and enhancements.

New Journal of Physics

The open access journal at the forefront of physics

PAPER

Prospects of temperature performance enhancement through higher resonant phonon transition designs in GaAs-based terahertz quantum-cascade lasers

Aleksandar Demić[*] ⬦, Zoran Ikonić ⬦, Paul Dean ⬦ and Dragan Indjin ⬦

School of Electronic and Electrical Engineering, University of Leeds, LS2 9JT, Leeds, United Kingdom
[*] Author to whom any correspondence should be addressed.

E-mail: A.Demic@leeds.ac.uk, Z.Ikonic@leeds.ac.uk, P.Dean@leeds.ac.uk and D.Indjin@leeds.ac.uk

Abstract

In this work we discuss terahertz quantum cascade laser designs that employ resonant phonon mechanism to assist the lasing process. We investigate whether the higher energy separation would be more beneficial for high temperature performance than commonly used resonant value of 36 meV (in GaAs). We show that our density matrix model can be used for reliable cut-off temperature estimation and we present design improvement of several exemplary structures by enhancing their material gain to attain 10–50 K higher cut-off temperature.

1. Introduction

Terahertz-frequency quantum cascade lasers [1–7] represent the pinnacle of semiconductor band-structure engineering, that have delivered powerful sources in traditionally hardly accessible far-infrared spectrum. The variety of designs [8] provide a wide range of lasing frequencies (1.2–5.6 THz [9–12]), high power performance [13] and operation up to 250 K [14] in pulsed and 129 K [15] in continuous wave (CW) operation (without the assistance of external magnetic field).

The potential applications span from free-space communications, medical diagnostics and chemical sensing [16–19] to state-of-the-art imaging using the external homodyne feedback [20–24].

A variety of materials and approaches are employed in order to improve the performance of QCLs [7, 25], and this must be underpinned by a good understanding of carrier transport within these devices. The dominant material system for THz QCLs is GaAs/AlGaAs due to its performance and technology level, however great interest is drawn by semiconductors with lower effective masses as InGaAs and InAs [26, 27] or higher longitudinal optical (LO) phonon energy such as GaSb and GaN [25, 28] and reliable and efficient modelling approaches are needed for further development of THz technology.

In terms of transport models [29], the semi-classical rate-equation (RE) models [30] neglect coherence effects and quantum mechanical dephasing and may generate non-physical output [31], while quantum models as Wigner function [32] and non-equilibrium Green's function approaches [33, 34], although most general, suffer from very high computational cost. The density matrix (DM) models [31, 35–38] offer the compromise with moderate computational requirements that provide reasonable description of THz QCL operation [37].

In this paper we focus on DM approach [31, 35] which employs infinite period consideration of QCL within the first neighbour and tight binding approximation. We consider various non-radiative interactions of electrons with alloy disorder, LO phonons, acoustic (AC) phonons, ionised impurities, interface roughness (IFR) and other electrons (EE). These scattering mechanisms are treated through the perturbation theory via Fermi-golden rule [39]. The robustness of similar model is discussed in [37], however here we focus on its ability of predicting cut-off temperature reliably and discuss devices for high temperature performance.

We provide detailed discussion on different THz QCL designs and investigate the paradigm shift introduced in the latest record performance [14] in terms of increasing the energy separation between states designed to assist the lasing process through LO-phonon scattering. This has also been noticed in earlier experimental works which focussed on barrier height optimisation [40] and temperature performance optimisation [41].

2. Cut-off temperature prediction

In previous work [42] we demonstrated the efficiency of DM model by simulating several million devices. These simulations relied on the capability of our [31,35] and similar [37] models to predict the cut-off temperature of different designs for any number of states per module.

Our simulation procedure comprises electronic structure calculation by solving the Schrödinger–Poisson equation under tight binding approximation in self–self-consistent manner and employing DM model for electron transport modelling. The DM model is formulated by Liouville equation within the nearest neighbour approximation where coherent interaction between adjacent QCL periods uses the model from [43] to obtain Rabi coupling energies. The key aspect of our DM approach is that the dissipator term in Liouville equation superoperator [35] uses scattering rates calculated by Fermi-golden rule that are averaged over Fermi–Dirac distribution at electron temperature. We employ scattering mechanism calculation that is described in detail in [39] we use equithermal subband approximation for solving the kinetic balance equation and obtaining the electron temperature. This approach [30, 44] transforms the kinetic balance equation into a minimization problem with one unknown, rather than the nonlinear system [37, 45] with subband temperatures as the unknowns. Therefore our model consists of iterative algorithm (the Schrödinger–Poission solver) nested within the minimization algorithm for determination of electron temperature. What couples these two algorithms together is the underlying DM transport model, which provides subband populations required for Schrödinger–Poission solver and requires scattering rates obtained via Fermi golden rule and averaged by Fermi–Dirac distribution at electron temperature [39, 44] Note that although equithermal subband approximation is seemingly robust, we still have a very high quality of cut-off temperature predictions as models that calculate all subband temperatures [37].

Our algorithm for determination of cut off temperature is explained in detail and illustrated with an example in the supplementary material (https://stacks.iop.org/NJP/24/033047/mmedia) (https://doi.org/10.5518/1101), and it consists of the following steps

- Set lattice temperature T_0 and electrical bias K_0.
- Extract material gain dependence on frequency f, $g(f, T_0, K_0)$. The peak of this dependence represents the lasing gain and corresponding frequency f_{max} is the lasing frequency.
- Sweep electrical bias to obtain $g(f_{max}, T_0, K)$ and the corresponding current density $J(T_0, K)$. The peaks of $g(f_{max}, T_0, K)$ occur at bias K_{max} which represents the resonant bias. The peaks of $J(T_0, K)$ occur at bias K_{NDR} and this corresponds to the case when the structure exhibits non differential resistance (NDR) behaviour, and this is usually when lasers abruptly stops lasing in the experiment.
- Sweep temperature to extract $g_{max}(T) = g(f_{max}, T, K_{max})$ and $g_{NDR}(T) = g(f_{max}, T, K_{NDR})$. It applies that $g_{NDR}(T) \leqslant g_{max}(T)$, thus using $g_{NDR}(T)$ to estimate the cut-off temperature is stricter condition, and thus more reliable for temperature optimisation [42].

Figure 1 displays the gain dependence on temperature for several significantly different QCL designs thus illustrating the versatility of our DM model. The bottom dotted red line represents the total waveguide loss in metal–metal waveguide configuration which is taken as 20 cm^{-1} for structures lasing at 3–4 THz and 40 cm^{-1} for 1.2 THz design as we expect significantly higher loss at lower frequency [49]. The top dotted red line can be attributed to electrical heating (and use of different duty cycles) and is added to create an expected cut-off temperature region. We can observe that nearly all devices have reached 20 cm^{-1} limit very close to the experimental cut-off value. We may also argue that mismatches in figure 1(c) are due to use of 10% duty cycle in [12], and figure 1(b) performs better in experiment than expected due to very low duty cycle (and waveguide loss at 4 THz being less than 20 cm^{-1} [49]).

In previous work [42], we discussed the temperature degradation mechanisms and introduced the effective level schematics of common QCL devices which may help to simplify the design by considering clusters of narrow states as single 'miniband' states. The benefit of such minibands can be viewed in figures 1(c), (d) and (f) as they serve to better inject the carriers into adjacent QCL period (material gain at low temperature would thus be higher) and to lower the resonant bias (and therefore voltage) which would reduce the electrical heating and provide better CW performance. The dual phonon design, figure 1(f), needs very high voltage drop to align resonant states and this was prevented in [9] by using two consecutive
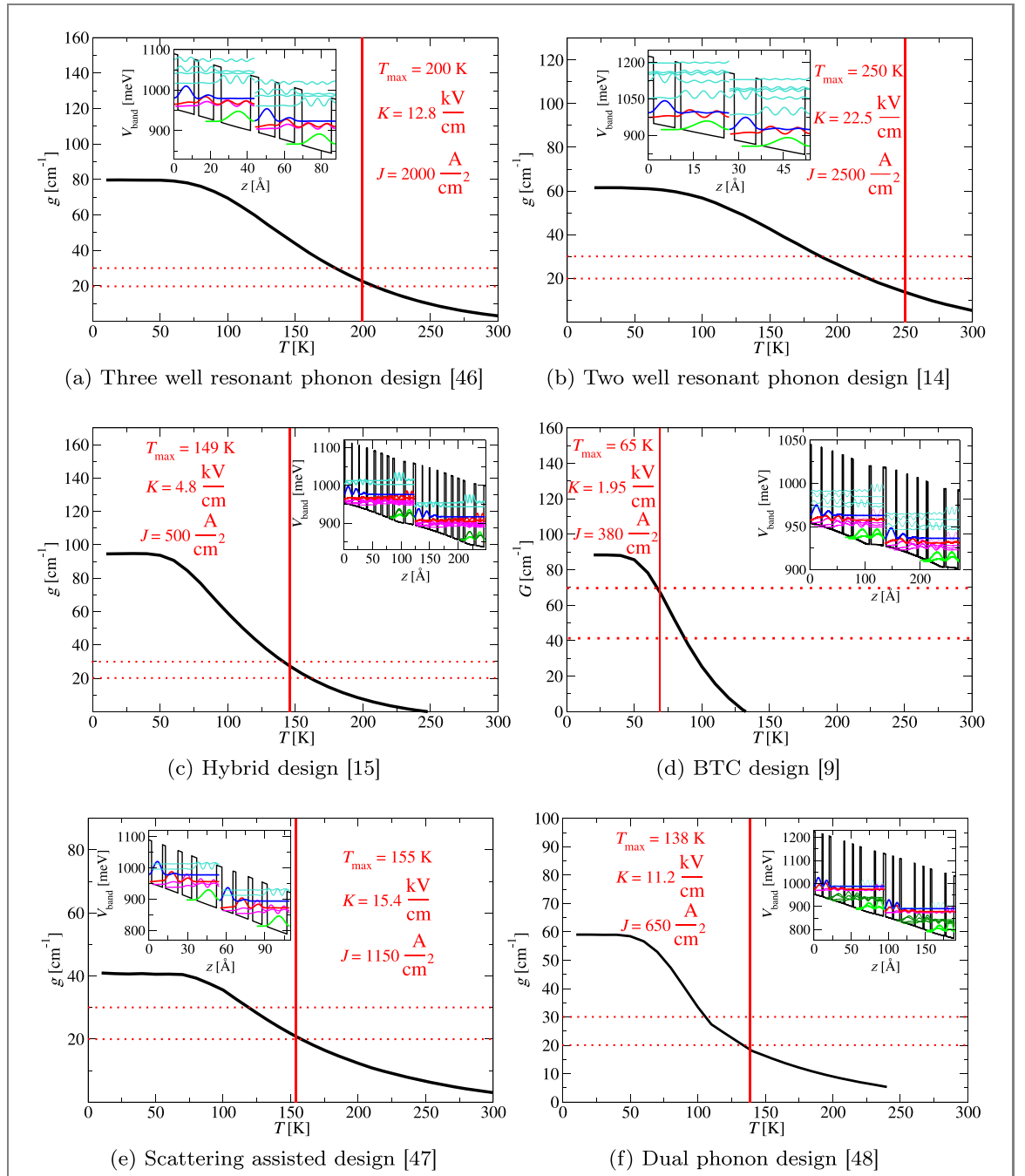
Figure 1. Material gain dependence on temperature at the corresponding resonant bias of several QCL devices: (a) former 200 K record temperature design under pulsed operation [46], (b) current 250 K record temperature design [14] pulsed operation, (c) current 129 K record design under CW operation [15], (d) the lowest frequency (1.2 THz) design [9], (e) scattering assisted design [47], (f) dual phonon design [48]. Inset shows the corresponding bandstructure and wavefunctions moduli, the dotted horizontal lines roughly depict the cut-off temperature expectation while the horizontal red line represents the experimental cut-off temperature at pulsed operation.

minibands separated by resonant LO-phonon energy. The main drawback of minibands is that at high temperature the number of non-radiative interactions would increase, leading to faster material gain degradation than in designs with fewer quasi-bound states. For this reason, generating or optimizing a QCL design should not be conducted only at low temperature.

Note that regardless of the QCL design in figure 1, the material gain dependence on temperature (at the design bias) contains 'flat' and monotonically decreasing regions. The better structures have the latter region more linear, with smaller slope. The linearity and the slope of this region is better in designs with fewer states and more separated parasitic higher states. With this in mind, the initial two well improvement of the resonant phonon design [50] has increased the cut-off temperature only to 210 K, and the reason of the current record design success lies in changing the established paradigm of designing extraction level with energy separation equal to the resonant LO-phonon energy.

We should also point out that results in figure 1 do not provide information on effect of temperature change on the entire dynamical range. Figure 1 only considers the peak material gain (or at NDR point). This therefore disregards impact of electrical bias on level misalignment and does not offer information on how dynamic range is affected with the temperature increase.

3. LO-phonon leakage

The critical parameter of LO-phonon scattering is the resonant energy $\hbar\omega_{LO}$ (36 meV in GaAs). It is expected that if two quasi-bound states in QCL structure are separated by this amount, the LO-phonon scattering would be dominant and for that reason this process has been used to assist either pumping of upper lasing level (ULL) or more commonly, depopulation of the lower lasing level (LLL).

Traditionally, QCL designs used ∼36 meV separation, although a simple simulation of a single quantum well indicates that this mechanism persists at higher temperatures with higher energy separation [39]. In figure 2 we conducted similar simulation as in [39] where we varied quantum well width and used self-consistent Schrödinger–Poisson solver to determine the averaged scattering rate between first two quasi-bound states. We varied the well width with no external electric bias and averaging of the scattering rate was done via Fermi–Dirac distribution at lattice temperature. This means that if one wants to relate this result to a QCL, higher electron temperature would correspond to lower lattice temperature.

We can observe two forms of LO-phonon leakage that can occur at high temperature in figure 2. At high energy LO-phonon leakage can persist even over 60 meV after the resonance at 36 meV. At low energy (<20 meV), LO-phonon scattering will also rise with temperature. This is a substantial hazard if we envision a three level resonant phonon QCL design. In the inset in figure 2(b) we illustrated LO-phonon leakage effects at 14.4, 36, and 50.6 meV which would typically correspond to 3.5 THz structure designed with three levels. It is clear that ULL could leak towards the ground level, and also scatter non-radiatively to LLL. Note however, that figure 2 corresponds to a single quantum well with no external bias, thus the dipole matrix element is high for all energy differences which may not be the case in biased quantum well systems as in QCL. In fact, although severe in the first instant, LO-phonon leakage at high energy in QCL may be mild as typically ULL does not overlap with the ground level significantly. On the other hand, temperature performance of THz QCLs is dictated by LO-phonon leakage at lasing and low energy [51].

Apart from BTC 1.2 THz design in figure 1, all presented structures employ LO-phonon scattering transition to assist the lasing process. In figure 3 we present relevant LO-phonon scattering rates for the three well resonant phonon design in figure 1(a). LO-phonon scattering between first three states, W_{31} and W_{21}, is highly desired as this depopulates the LLL, while all transitions from ULL via LO-phonon scattering mechanism represent LO-phonon leakage. We can observe in figure 3 that ULL does not leak significantly towards the ground state as W_{41} is negligible mainly due to large energy separation (56.5 meV) and very small dipole matrix element, however ULL scatters to LLL and the second state as temperature increases. Note that the scale of LO-phonon leakage at low energy in figure 3 seems to be low, however if we compare the material gain degradation with temperature from the full model in figure 1(a), we can see that the temperature dependence of the material gain directly correlates to the linearity of the leakage process between the lasing states as desired resonant phonon transitions do not have rapid change of the scattering rate with temperature.

We observed similar behaviour of LO-phonon scattering dependence on temperature, between the lasing states, for all designs in figure 1. A clear solution for LO-phonon leakage at low energy would be changing the material system as we expect similar results as in figure 2, but shifted towards higher resonant energy value. In terms of the design, we cannot prevent this mechanism as there is a trade-off concerning the dipole matrix element and improvement strategies would be reduction of quasi-bound states around ULL, optimizing the dipole moment between ULL and LLL, or having more efficient pumping/extraction mechanisms.

4. Design improvement with LO-phonon transitions at higher energy

The most recent temperature record structure [14] has been designed with the extraction energy separation of 50.4 meV to avoid LO-phonon leakage, high barriers ($x = 0.3$) to suppress formation of high parasitic states (the fourth state is 60.3 meV above ULL) and two wells in order to create the three level system. The only drawback of this design is its very high threshold which emerged as a consequence of necessary trade-offs: a high barrier structure requires higher doping density (this structure has 50% larger sheet doping density than [46]) and a two well design with resonant energy difference of 68.4 meV requires very large resonant bias (22.5 kV cm^{-1}). This was compensated by using very low duty cycle.
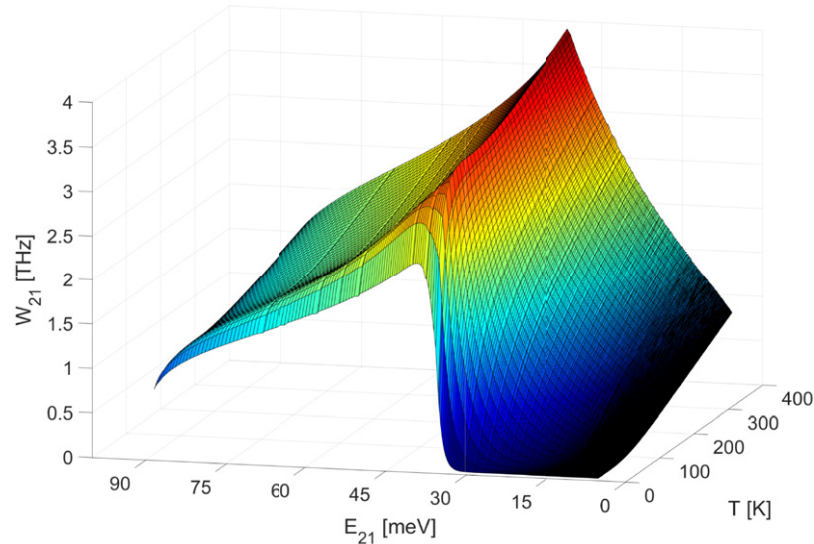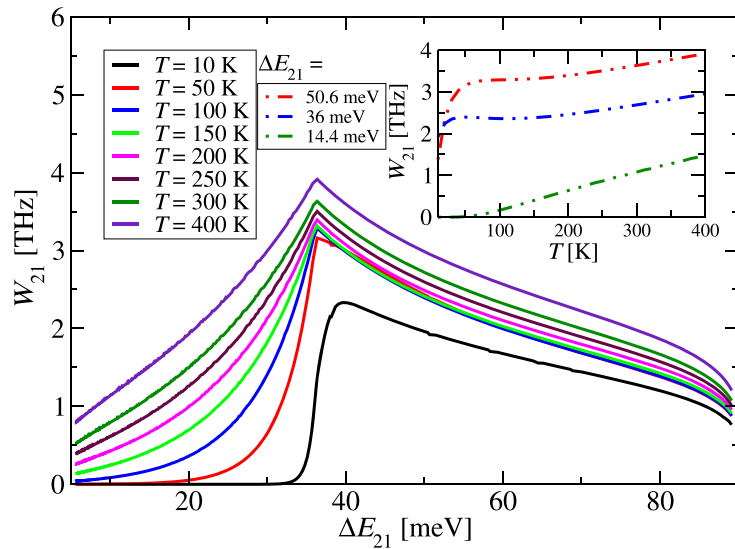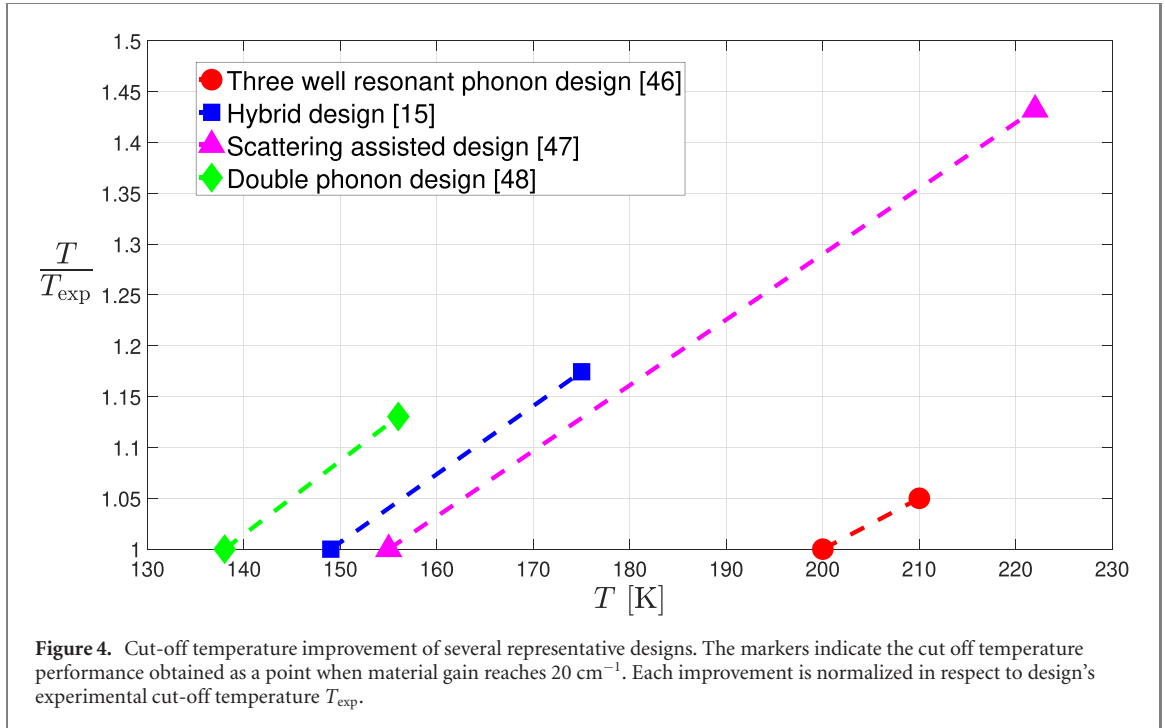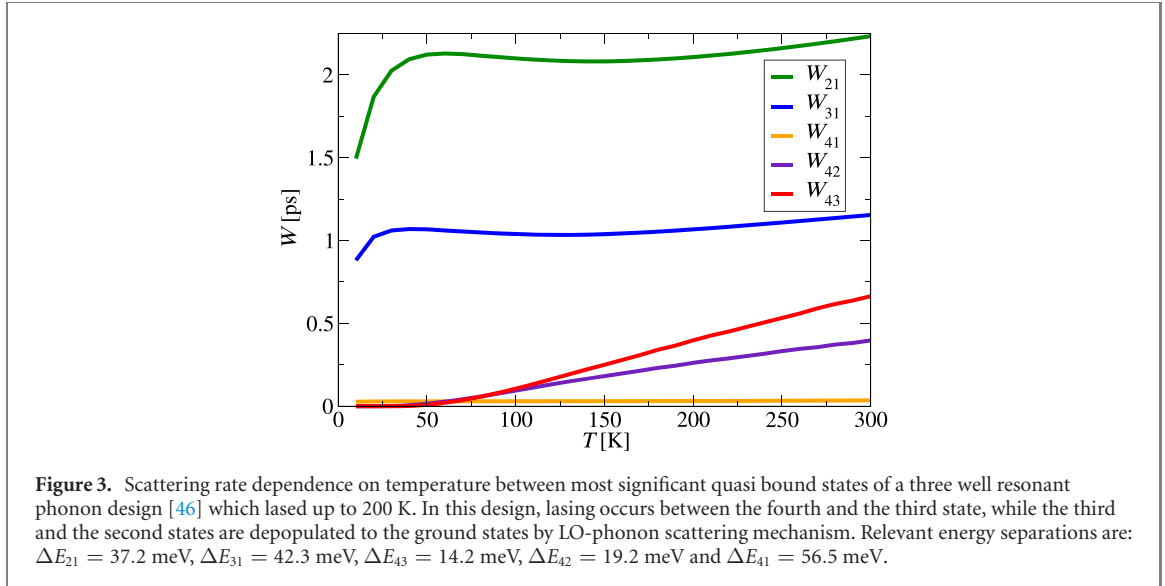
Figure 2. Averaged electron–LO-phonon scattering rate between first two quantum states of a single quantum well with no external bias. Bottom figure in (b) represents cross section of the top figure in (a). Inset in figure (b) shows dependence of scattering rate on temperature when energy difference is fixed. Averaging of the scattering rate was done at the lattice temperature.

There were several experimental works that have discussed whether the optimal value of LO-phonon transition should be higher. Work in [40] has explored the effect of barrier height on a particular design which inadvertently increased the transition above 36 meV and work in [41] directly investigated whether optimal design value should be focussed at 40 meV for a particular three well structure. The most recent temperature record of 250 K [14] is the first experimental demonstration that employed 51 meV LO-phonon transition and thus addressed the LO-phonon leakage issues at high temperature and it is worth considering whether temperature performance of other designs can be improved further to suppress leakage of ULL towards other levels. Only BTC design in figure 1 cannot benefit from this, as its operating principle is based on energies being below the resonant phonon energy.

We employed our highly efficient DM model to vary several layers in each design in similar fashion as in [42]. We kept Al molar fraction to 0.15 as in original designs, as our aim was not to generate optimized structures, but rather to provide a proof of concept that resonant phonon transitions >36 meV would be more beneficial. Cut-off temperature improvement is shown in figure 4 and changes in relevant quasi-bound levels' spacing for each design are presented in table 1.

The three well resonant phonon design [46] layer structure (starting from the injection barrier) is **43**/89/**24.6**/81.5/**41**/55/*50*/55 Å where layers in bold are barriers and the italicized well is doped to

Figure 3. Scattering rate dependence on temperature between most significant quasi bound states of a three well resonant phonon design [46] which lased up to 200 K. In this design, lasing occurs between the fourth and the third state, while the third and the second states are depopulated to the ground states by LO-phonon scattering mechanism. Relevant energy separations are: $\Delta E_{21} = 37.2$ meV, $\Delta E_{31} = 42.3$ meV, $\Delta E_{43} = 14.2$ meV, $\Delta E_{42} = 19.2$ meV and $\Delta E_{41} = 56.5$ meV.

Figure 4. Cut-off temperature improvement of several representative designs. The markers indicate the cut off temperature performance obtained as a point when material gain reaches 20 cm^{-1}. Each improvement is normalized in respect to design's experimental cut-off temperature T_{exp}.

6×10^{16} cm^{-3}. The improved structure has layer sequence **43**/87.6/**24.6**/70.6/**39.5**/49.8/**50**/49.8 Å where altered layers are highlighted in red. The resonant bias is $K = 14$ kV cm^{-1} and estimated cut-off temperature is increased to 216 K. Note that this structure has already been optimized for high temperature performance and it held the pulsed operation temperature record at 200 K for a long time. As discussed earlier, in figure 3 the ULL leaks towards LLL and the second state, and we believe that the change of LO-phonon transition between first two states from 37.2 to 40.3 meV was not the cause of slight improvement in figure 4, but rather the fact that ΔE_{43} and ΔE_{42} is lower in improved design, as we expect less LO-phonon leakage at lower energy as shown in figure 2.

The Hybrid design [15] layer structure (starting from the injection barrier) is **38**/118/**5**/118/**10**/124/**19**/113/**29**/91/**29**/82/**29**/68/**29**/163/**29**/139 Å where layers in bold are barriers and the italicized well is doped to 3×10^{16} cm^{-3}. The improved structure has layer sequence **38**/118/**5**/115/**10**/118/**19**/110/**29**/91/**29**/82/**29**/65/**29**/159/**29**/142 Å, where altered layers are highlighted in red (and italicized well is doped to 3.07×10^{16} cm^{-3}). The resonant bias is $K = 5.4$ kV cm^{-1} and estimated cut-off temperature is increased to 175 K. The inset in figure 1(c) depicts that this is a complex design which combines the BTC design principles with resonant phonon design, aiming to achieve high temperature performance under CW operation. The first two levels are narrowly spaced and separated

Table 1. Energy difference change between relevant quasi-bound states in exemplary structures before and after layer variation. The lasing transition is highlighted in red.

Design	Relevant ΔE_{ij} [meV]	Altered ΔE_{ij} [meV]
[46]	$\Delta E_{21} = 37.2$	$\Delta E_{21} = 40.3$
	$\Delta E_{42} = 19.4$	$\Delta E_{42} = 18.6$
	$\Delta E_{43} = 14.3$	$\Delta E_{43} = 12.7$
[15]	$\Delta E_{41} = 35.7$	$\Delta E_{41} = 38.8$
	$\Delta E_{31} = 32.3$	$\Delta E_{31} = 34.9$
	$\Delta E_{32} = 29.8$	$\Delta E_{32} = 31.5$
	$\Delta E_{11,9} = 13.4$	$\Delta E_{11,9} = 14.3$
[47]	$\Delta E_{21} = 40.4$	$\Delta E_{21} = 29.4$
	$\Delta E_{31} = 46.6$	$\Delta E_{31} = 66.3$
	$\Delta E_{54} = 21.8$	$\Delta E_{64} = 32.8$
	$\Delta E_{43} = 8.83$	$\Delta E_{43} = 11.8$
[48]	$\Delta E_{31} = 35.7$	$\Delta E_{31} = 42.6$
	$\Delta E_{32} = 30.2$	$\Delta E_{32} = 35.8$
	$\Delta E_{61} = 51.3$	$\Delta E_{61} = 61.1$
	$\Delta E_{76} = 30.6$	$\Delta E_{86} = 37.7$
	$\Delta E_{96} = 35.6$	$\Delta E_{96} = 42$
	$\Delta E_{11,9} = 15.3$	$\Delta E_{11,9} = 16.9$

from a six level miniband of higher states by 36 meV on average. This design clearly suffers from multiple LO-phonon leakage transitions and the improved design which shifted the miniband separation from the ground level to $\sim$40 meV on average has improved material gain profile. Note that we focussed on improving the temperature performance under pulsed operation even though this structure currently holds the record for the highest temperature CW operation. We believe that further design study could generate more optimized structure, however this represents a numerical challenge even for our own efficient DM model as it is not feasible to vary all layers of a nine-well structure simultaneously.

The scattering assisted design [47] layer structure (starting from the injection barrier) is **42**/85/**23**/96/**34**/73/**40**/*153* Å, where layers in bold are barriers and the italicized well is doped to 2.05×10^{16} cm^{-3}. The improved structure has layer sequence **42**/67.8/**23**/96/**34**/73/**40**/206.2 Å, where altered layers are highlighted in red and italicized well is doped to 1.52×10^{16} cm^{-3}. The resonant bias is $K = 20.3$ kV cm^{-1} and estimated cut-off temperature is increased to 222 K. This design employs two resonant phonon transitions to both pump the ULL and extract the LLL. This design already has separation between the first two levels >36 meV, however the fifth state that was intended to pump ULL is separated by 21.8 meV from it, as this is a 1.8 THz structure, the fifth state is therefore separated from LLL by 30.6 meV. It is clear that the fifth state would pump both lasing levels, which is why the design improvement generated significantly better cut-off temperature estimation. Note that the improved design has a ladder of two consecutive states with separation of roughly 30 meV and state above ULL is also separate by a similar amount, therefore creating a somewhat different scattering assisted structure.

The double phonon design [48] layer structure (starting from the injection barrier) is **31**/93/**14**/82/**23**/175/**11**/105/**14**/85/**20**/*175*/**17**/105 Å where layers in bold are barriers and the italicized well is doped to 2.8×10^{16} cm^{-3}. The improved structure has layer sequence **31**/93/**14**/73.4/**23**/155.4/**11**/110.2/**14**/84.7/**20**/*155.4*/**17**/110.1 Å, where altered layers are highlighted in red (and italicized well is doped to 3.15×10^{16} cm^{-3}). The resonant bias is $K = 12.7$ kV cm^{-1} and estimated cut-off temperature is increased to 155 K. Improvement of this design has already been theoretically explored in [52]. Similarly to the hybrid design, this structure employs large number of quasi-bound states in order to create two consecutive minibands spaced by $\sim$36 meV. The improved design increased this spacing, resulting in a slightly better structure, however due to very large number of states, this design overall suffers from LO-phonon leakage at low energy.

5. New designs with high LO-phonon transitions

In the previous section we discussed design improvement of existing devices that were mostly using barriers with 0.15 Al molar fraction. The increase of transition energy in table 1 generated devices with roughly $\sim$ 40 meV which is in a good agreement with previous experimental work in [41]. However structure [14] has demonstrated a two well design with 51 meV transition energy and barriers with 0.3 Al molar fraction
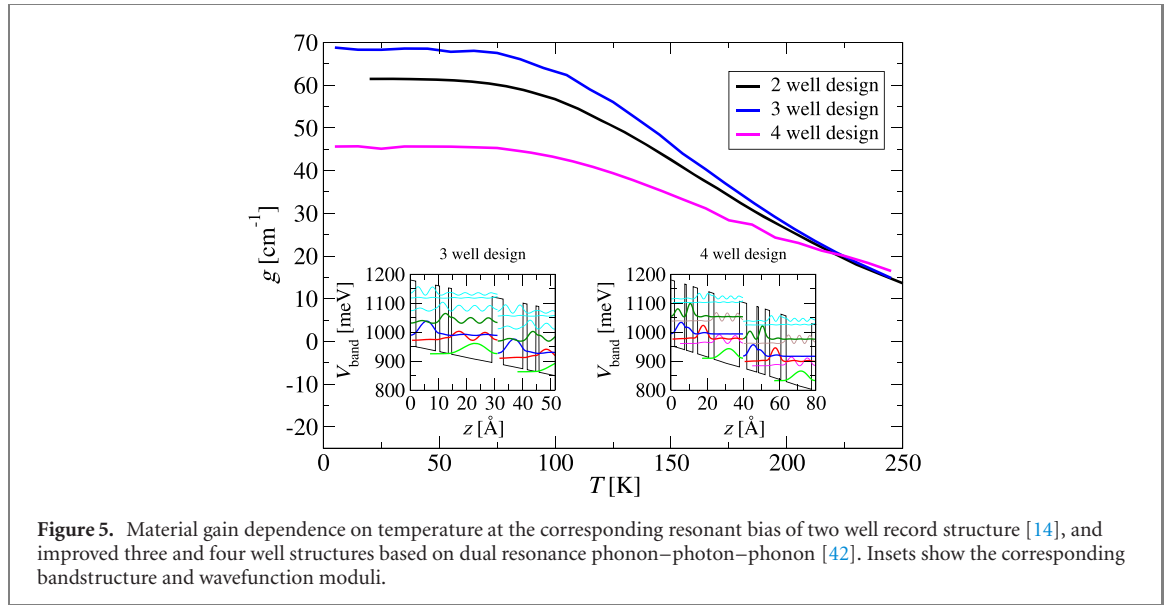
Figure 5. Material gain dependence on temperature at the corresponding resonant bias of two well record structure [14], and improved three and four well structures based on dual resonance phonon–photon–phonon [42]. Insets show the corresponding bandstructure and wavefunction moduli.

which lased up to 250 K. It is clear that there is benefit in employing both of these strategies as higher barriers would reduce parasitic leakage and we would also be able to easily generate structures with higher transition energies. In designs discussed so far, we can not increase this energy further as the barriers are low and we would require higher resonant bias. This would lead to a device where there is more pronounced hazard of parasitic leakage via higher states.

In our previous work [42] we proposed a new type of design that exploits two resonant phonon transitions, one above the ULL to assist its pumping, and one below the LLL to assist its extraction. In [42] we focussed on avoiding structures with high LO-phonon energy transitions due to higher threshold current. Due to recent success of [14] we have repeated our optimisation procedure with barriers with $x = 0.25$ Al molar fraction, and noticed the overwhelming benefits of designs with transitions > 45 meV. The following designs have shown the most promise:

- Three well structure, with layer sequence starting from the injection barrier (assuming bandstructure potential tilt to the right): **39.55**/70.625/**14.125**/31.075/**11.3**/*144.075* Å where $Al_{0.25}Ga_{0.75}As$ barriers are shown in bold text, wells in normal text and central 30 Å of the italicized third well has been doped to 1.5×10^{17} cm^{-3}, with resonant bias $K = 20$ kV cm^{-1}. This design has the following energy transitions $\Delta E_{21} = 46.2$ meV, $\Delta E_{32} = 16.3$ meV, $\Delta E_{43} = 42.8$ meV, $\Delta E_{54} = 40.9$ meV and $\Delta E_{65} = 46.3$ meV.

- Four well structure, with layer sequence starting from the injection barrier (assuming bandstructure potential tilt to the right): **39.55**/56.5/**8.475**/36.725/**25.425**/62.15/**28.25**/*141.25* Å where $Al_{0.25}Ga_{0.75}As$ barriers are shown in bold text, wells in normal text and central 30 Å of the italicized fourth well has been doped to 1.5×10^{17} cm^{-3}, with resonant bias $K = 19.5$ kV cm^{-1}. This design has the following energy transitions $\Delta E_{21} = 51.2$ meV, $\Delta E_{32} = 14.7$ meV, $\Delta E_{43} = 17.9$ meV, $\Delta E_{54} = 44.26$ meV and $\Delta E_{65} = 14.6$ meV.

In figure 5 we can see that both of these designs compare very well with the current record design [14] (they all intersect gain of 20 cm^{-1} around $T = 225$ K). Both of these design employ dual resonance phonon–photon–phonon scheme, in three well design $\Delta E_{21} = 46.2 \approx \Delta E_{43} = 42.8$ meV and in four well design $\Delta E_{31} = 65.9 \approx \Delta E_{64} = 60.8$ meV. The expected lasing frequency of three well design is 3.9 THz, and of four well design is 4.3 THz.

Both of these novel designs display very interesting features. The three well design has all consecutive energy transitions (apart from the lasing one) close to resonant phonon energy (in range 40–47 meV), while the four well design displays transition at very high energy (>60 meV) and displays significantly better gain degradation slope than two and three well design in figure 5. This also reveals a potential hazard of designing QCL with high LO-phonon transitions. The LO-phonon mechanism is dominant at high temperature, thus the slope improvement of the four well design is expected, however, this mechanism is not dominant at low temperature, and such design may have an issue operating well at low temperatures. The material gain of four well structure is ~ 45 cm^{-1} which is fairly low and suitable only for double metal waveguides. This can be somewhat compensated with higher doping, which would also increase the current density and create another trade-off to be considered.

6. Conclusion

In this work we investigated critical effects that cause the material gain degradation with temperature by using our DM model for high quality prediction of cut-off temperature performance of THz QCLs.

We illustrated two forms of LO-phonon leakage that can occur either at low energy or above the resonant energy and showed that former effect is dominant due to low lasing energy in THz structures. Although this cannot be rectified without a different material system (with higher resonant LO-phonon energy), we can still engineer some design improvement in GaAs/AlGaAs structures by suppressing the leakage of ULL towards other lower levels which is also present, especially if dipole matrix element is not negligible.

The most recent record of pulsed operation up to 250 K [14] was achieved by somewhat unusual QCL design which used 51 meV energy separation for LO-phonon transition. We therefore investigated whether the concept of designing structure with desired transitions at resonant phonon energy (36 meV) should be changed.

We employed our DM model and varied several layers of four distinct QCL designs to verify that larger energy spacing between desired LO-phonon transitions is beneficial. However there are several trade-offs to be considered, as structures with higher energy spacing typically have higher threshold, worse performance at low temperature and, due to formation of high states, higher barrier quantum well system may be required.

As supportive examples, we proposed two structures that employ dual resonance phonon–photon–phonon design [42] with transitions energies that are higher or comparable to the record operation temperature design [14]. Both of these designs promise comparable or better material gain degradation profile than the reference structure [14].

Overall, degradation of material gain is caused by LO-phonon scattering of ULL towards any level with which ULL has non-negligible dipole moment. Engineering desired resonant phonon transitions above resonant energy value does bring some benefit, however as ULL would always have a significant dipole moment with LLL, it is clear that in THz spectrum, temperature performance is dictated by LO-phonon leakage at low energy and this can only be rectified by using prospective material system with higher resonant phonon energy, even if the optimized new design proposals [42] are experimentally successful.
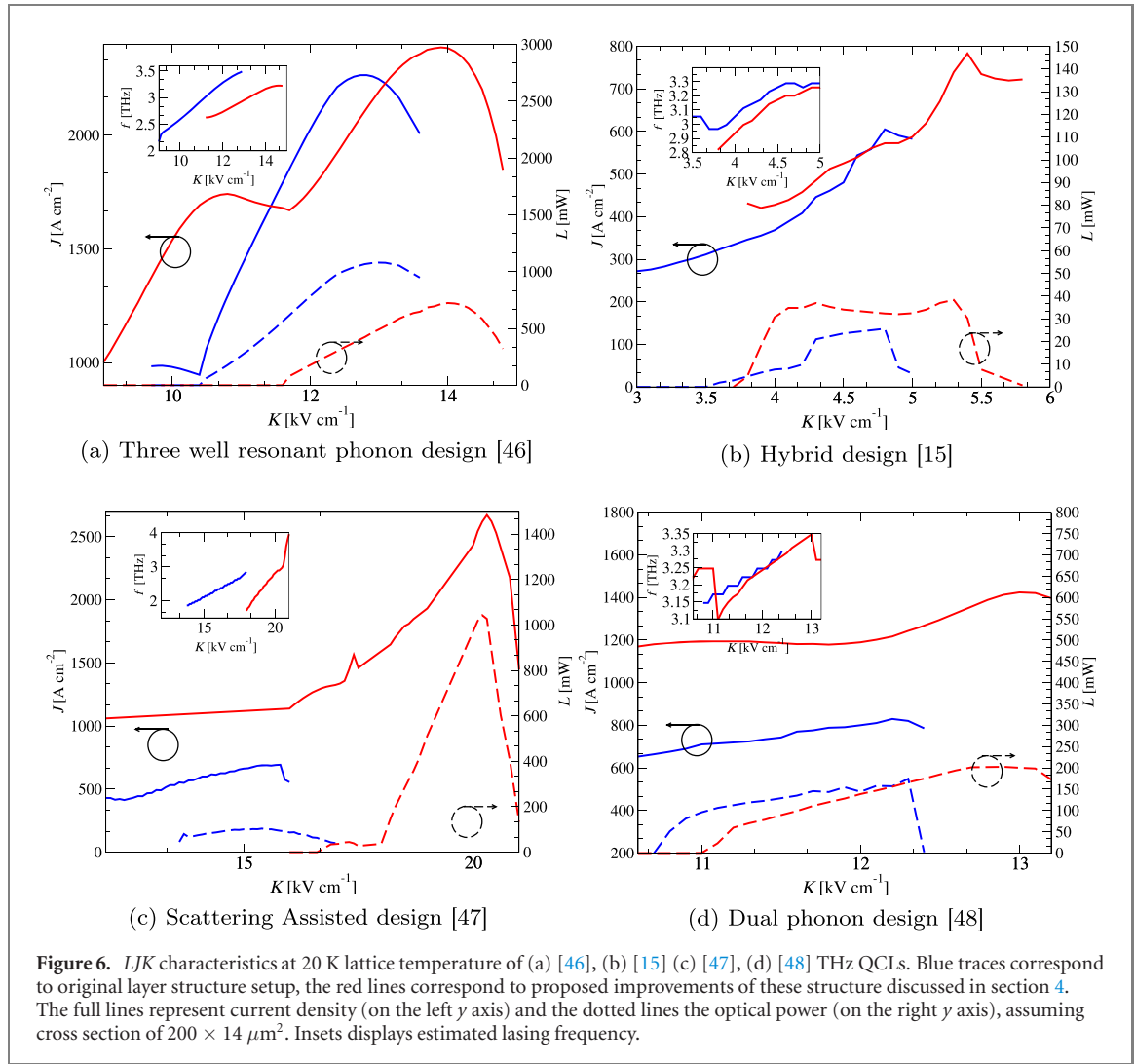
Acknowledgments

Data availability statement

The data that support the findings of this study are available upon reasonable request from the authors.

Appendix A. Detail performance comparison

In section 4 we have discussed device improvement based on its material gain at resonant bias, which is the most relevant factor for estimating the cut-off temperature. This approach does not give full insight on how other relevant performance factors are affected by change of design layers. All improved versions of existing designs operate on different resonant bias, have different quasibound state energies and therefore it is expected that along with their cut-off temperature predictions, other relevant performance parameters are changed as well.

In [31] we have demonstrated our fitting procedure to the experimental results, however in this work, we have not fitted any structure in figure 1 to their experimental counterpart, as our fitting parameters (IFR correlation length and height) are tied to IFR scattering mechanism which becomes negligible at higher temperatures. This property of our model allowed us to predict cut-of temperatures in figure 1 with ease, but this is responsible for some robustness of our approach in terms of the initial value of material gain from which the curves in figure 1 start decaying.

In [35] we briefly discussed our dynamic DM model where we upgraded our model in terms of calculating the optical power (and seeing its dynamics). We found in [53] that the values we are getting for

Figure 6. *LJK* characteristics at 20 K lattice temperature of (a) [46], (b) [15] (c) [47], (d) [48] THz QCLs. Blue traces correspond to original layer structure setup, the red lines correspond to proposed improvements of these structure discussed in section 4. The full lines represent current density (on the left *y* axis) and the dotted lines the optical power (on the right *y* axis), assuming cross section of $200 \times 14 \ \mu m^2$. Insets displays estimated lasing frequency.

magnitude of optical power agree very well to the experimental ones, if detection efficiency of 15%–25% is assumed.

The performance of referent and improved structures may be of interest for experimental realization of improved designs, thus in this appendix we will provide detail *LJK* comparison of designs discussed in the paper. Note that we decided for *LJK* graphs instead of *LIV*, because it is a matter of scaling electric bias *K* and current density *J* with device dimension and it avoids additional fitting of voltage through contact resistance parameter. Our model calculates magnitude of optical electrical field as steady state value from our dynamic model with assumed waveguide loss of 20 cm^{-1}. We can then estimate the optical intensity and scale this value with device dimensions to obtain optical power *L*, we will assume device dimensions of $200 \times 14 \ \mu m^2$ in our calculations.

In figure 6 we have not displayed the material gain dependence on bias, but rather the optical power. Note that as improved design have different layer widths, the optical power may not necessarily be larger in improved design proposals. The structures in figure 1 illustrated the decay of the peak (or at NDR point if smaller) material gain with temperature. The proposed improvements in section 4 have been optimized to increase the cut-off temperature of the original designs. However this increase does not illustrate how the transport of the device is affected.

In figure 6(a), we can notice that improved design has higher threshold, similar dynamic range, and lower optical power than the reference structure. Hybrid structure in figure 6(b) operates with larger dynamic range and higher current density. The scattering assisted design in figure 6(c) is significantly different than its reference [47] mainly because of significantly different bandstructure. In table 1, the improved design has $\Delta E_{21} = 29.4$ and $\Delta E_{31} = 66.3$ meV in contrast to the former values of $\Delta E_{21} = 40.4$ and $\Delta E_{31} = 66.6$ meV. The improved design is also more likely to lase at higher frequency. The dual phonon design in figure 6(d) mainly has higher threshold.

All results in figure 6 are presented at 20 K. The aim of this work was to improve the cut-off temperature of each design, and this is ensured by study of graphs similar to figure 1. The improved designs have better

material gain degradation with temperature, however as it can be seen in figure 6 their threshold, optical power, dynamic range and frequency would be different than the reference designs.

ORCID iDs

Aleksandar Demić ⬤ https://orcid.org/0000-0003-1335-6156
Zoran Ikonić ⬤ https://orcid.org/0000-0003-4645-377X
Paul Dean ⬤ https://orcid.org/0000-0002-3950-4359
Dragan Indjin ⬤ https://orcid.org/0000-0002-9121-9846

References

[1] Kazarinov R F and Suris R A 1971 Possibility of amplification of electromagnetic waves in a semiconductor with superlattice *Sov. Phys.-Semicond.* **5** 707–9

[2] Faist J, Capasso F, Sivco D L, Sirtori C, Hutchinson A L and Cho A Y 1994 Quantum cascade laser *Science* **264** 553–6

[3] Capasso F 2010 High-performance midinfrared quantum cascade lasers *Opt. Eng.* **49** 111102

[4] Köhler R, Tredicucci A, Beltram F, Beere H E, Linfield E H, Davies A G, Ritchie D A, Iotti R C and Rossi F 2002 Terahertz semiconductor-heterostructure laser *Nature* **417** 156–9

[5] Williams B S 2007 Terahertz quantum-cascade lasers *Nat. Photon.* **1** 517

[6] Tonouchi M 2007 Cutting-edge terahertz technology *Nat. Photon.* **1** 97

[7] Kumar S 2011 Recent progress in terahertz quantum cascade lasers *IEEE J. Sel. Top. Quantum Electron.* **17** 38–47

[8] Kumar S *et al* 2007 Development of terahertz quantum-cascade lasers *PhD Thesis* Massachusetts Institute of Technology

[9] Walther C, Fischer M, Scalari G, Terazzi R, Hoyler N and Faist J 2007 Quantum cascade lasers operating from 1.2 to 1.6 THz *Appl. Phys. Lett.* **91** 131122

[10] Scalari G, Walther C, Fischer M, Terazzi R, Beere H, Ritchie D and Faist J 2009 THz and sub-THz quantum cascade lasers *Laser Photon. Rev.* **3** 45–66

[11] Chan C W I, Hu Q and Reno J L 2012 Ground state terahertz quantum cascade lasers *Appl. Phys. Lett.* **101** 151108

[12] Wienold M, Röben B, Lü X, Rozas G, Schrottke L, Biermann K and Grahn H T 2015 Frequency dependence of the maximum operating temperature for quantum-cascade lasers up to 5.4 THz *Appl. Phys. Lett.* **107** 202101

[13] Li L, Chen L, Zhu J, Freeman J, Dean P, Valavanis A, Davies A G and Linfield E H 2014 Terahertz quantum cascade lasers with >1 W output powers *Electron. Lett.* **50** 309–11

[14] Khalatpour A, Paulsen A K, Deimert C, Wasilewski Z R and Hu Q 2021 High-power portable terahertz laser systems *Nat. Photon.* **15** 16–20

[15] Wienold M, Röben B, Schrottke L, Sharma R, Tahraoui A, Biermann K and Grahn H T 2014 High-temperature, continuous-wave operation of terahertz quantum-cascade lasers with metal–metal waveguides and third-order distributed feedback *Opt. Express* **22** 3334–48

[16] Gmachl C, Capasso F, Sivco D L and Cho A Y 2001 Recent progress in quantum cascade lasers and applications *Rep. Prog. Phys.* **64** 1533

[17] Kosterev A A and Tittel F K 2002 Chemical sensors based on quantum cascade lasers *IEEE J. Quantum Electron.* **38** 582–91

[18] Wysocki G *et al* 2008 Widely tunable mode-hop free external cavity quantum cascade lasers for high resolution spectroscopy and chemical sensing *Appl. Phys.* B **92** 305–11

[19] McManus J B, Shorter J H, Nelson D D, Zahniser M S, Glenn D E and McGovern R M 2008 Pulsed quantum cascade laser instrument with compact design for rapid, high sensitivity measurements of trace gases in air *Appl. Phys.* B **92** 387

[20] Leng Lim Y *et al* 2011 Demonstration of a self-mixing displacement sensor based on terahertz quantum cascade lasers *Appl. Phys. Lett.* **99** 081108

[21] Rakić A D *et al* 2013 Swept-frequency feedback interferometry using terahertz frequency QCLs: a method for imaging and materials analysis *Opt. Express* **21** 22194–205

[22] Lim Y L *et al* 2014 High-contrast coherent terahertz imaging of porcine tissue via swept-frequency feedback interferometry *Biomed. Opt. Express* **5** 3981–9

[23] Valavanis A *et al* 2012 Self-mixing interferometry with terahertz quantum cascade lasers *IEEE Sens. J.* **13** 37–43

[24] Dean P *et al* 2014 Terahertz imaging using quantum cascade lasers—a review of systems and applications *J. Phys. D: Appl. Phys.* **47** 374008

[25] Vitiello M S, Scalari G, Williams B and De Natale P 2015 Quantum cascade lasers: 20 years of challenges *Opt. Express* **23** 5167–82

[26] Ajili L, Scalari G, Hoyler N, Giovannini M and Faist J 2005 InGaAs–AlInAs/InP terahertz quantum cascade laser *Appl. Phys. Lett.* **87** 141107

[27] Brandstetter M *et al* 2016 InAs based terahertz quantum cascade lasers *Appl. Phys. Lett.* **108** 011109

[28] Detz H *et al* 2019 Evaluation of material systems for THz quantum cascade laser active regions *Phys. Status Solidi a* **216** 1800504

[29] Jirauschek C and Kubis T 2014 Modeling techniques for quantum cascade lasers *Appl. Phys. Rev.* **1** 011307

[30] Indjin D, Harrison P, Kelsall R W and Ikonic Z 2003 Self-consistent scattering model of carrier dynamics in GaAs–AlGaAs terahertz quantum-cascade lasers *IEEE Photon. Technol. Lett.* **15** 15–7

[31] Demic A *et al* 2017 Infinite-period density-matrix model for terahertz-frequency quantum cascade lasers *IEEE Trans. THz Sci. Technol.* **7** 368–77

[32] Jonasson O and Knezevic I 2015 Dissipative transport in superlattices within the Wigner function formalism *J. Comput. Electron.* **14** 879–87

[33] Yasuda H, Kubis T, Vogl P, Sekine N, Hosako I and Hirakawa K 2009 Nonequilibrium Green's function calculation for four-level scheme terahertz quantum cascade lasers *Appl. Phys. Lett.* **94** 151109

[34] Wacker A, Lindskog M and Winge D O 2013 Nonequilibrium Green's function model for simulation of quantum cascade laser devices under operating conditions *IEEE J. Sel. Top. Quantum Electron.* **19** 1–11

[35] Demić A, Ikonić Z, Kelsall R W and Indjin D 2019 Density matrix superoperator for periodic quantum systems and its application to quantum cascade laser structures *AIP Adv.* **9** 095019

[36] Burnett B A and Williams B S 2014 Density matrix model for polarons in a terahertz quantum dot cascade laser *Phys. Rev. B* **90** 155309

[37] Burnett B A, Pan A, Chui C O and Williams B S 2018 Robust density matrix simulation of terahertz quantum cascade lasers *IEEE Trans. THz Sci. Technol.* **8** 492–501

[38] Jonasson O, Karimi F and Knezevic I 2016 Partially coherent electron transport in terahertz quantum cascade lasers based on a Markovian master equation for the density matrix *J. Comput. Electron.* **15** 1192–205

[39] Harrison P and Valavanis A 2016 *Quantum Wells, Wires and Dots: Theoretical and Computational Physics of Semiconductor Nanostructures* (New York: Wiley)

[40] Kainz M A, Schönhuber S, Andrews A M, Detz H, Limbacher B, Strasser G and Unterrainer K 2018 Barrier height tuning of terahertz quantum cascade lasers for high-temperature operation *ACS Photonics* **5** 4687–93

[41] Baranov A N, Nguyen-Van H, Loghmari Z, Bahriz M and Teissier R 2019 Terahertz quantum cascade laser with non-resonant extraction *AIP Adv.* **9** 055214

[42] Demić A, Ikonić Z, Dean P and Indjin D 2020 Dual resonance phonon–photon–phonon terahertz quantum-cascade laser: physics of the electron transport and temperature performance optimization *Opt. Express* **28** 38788–812

[43] Yariv A, Lindsey C and Sivan U 1985 Approximate analytic solution for electronic wave functions and energies in coupled quantum wells *J. Appl. Phys.* **58** 3669–72

[44] Jovanović V, Höfling S, Indjin D, Vukmirović N, Ikonić Z, Harrison P, Reithmaier J and Forchel A 2006 Influence of doping density on electron dynamics in GaAs/AlGaAs quantum cascade lasers *J. Appl. Phys.* **99** 103106

[45] Kazemi-Tesieh M R, Yousefvand H R, Ghadimi A and Kiani-Sarkaleh A 2020 Terahertz generation in quantum-cascade lasers through down-conversion optical nonlinearity: design and modeling *Opt. Commun.* **468** 125792

[46] Fathololoumi S *et al* 2012 Terahertz quantum cascade lasers operating up to ∼200 K with optimized oscillator strength and improved injection tunneling *Opt. Express* **20** 3866–76

[47] Kumar S, Chan C W I, Hu Q and Reno J L 2011 A 1.8 THz quantum cascade laser operating significantly above the temperature of $\hbar\omega/k_B$ *Nat. Phys.* **7** 166

[48] Williams B S, Kumar S, Qin Q, Hu Q and Reno J L 2006 Terahertz quantum cascade lasers with double-resonant-phonon depopulation *Appl. Phys. Lett.* **88** 261101

[49] Han Y J *et al* 2018 Silver-based surface plasmon waveguide for terahertz quantum cascade lasers *Opt. Express* **26** 3814–27

[50] Bosco L, Franckié M, Scalari G, Beck M, Wacker A and Faist J 2019 Thermoelectrically cooled THz quantum cascade laser operating up to 210 K *Appl. Phys. Lett.* **115** 010601

[51] Indjin D, Harrison P, Kelsall R W and Ikonić Z 2003 Mechanisms of temperature performance degradation in terahertz quantum-cascade lasers *Appl. Phys. Lett.* **82** 1347–9

[52] Freeman W 2021 Double longitudinal-optical phonon intrawell depopulated terahertz quantum cascade structures: electron transport modeling using a density matrix method *Appl. Phys. Lett.* **118** 241107

[53] Demić A 2020 Density matrix modelling of terahertz frequency quantum cascade lasers: steady state analysis and Maxwell–Bloch dynamics *PhD Thesis* University of Leeds